Pure Appl. Geophys. 176 (2019), 1169–1191

https://doi.org/10.1007/s00024-018-1988-5

Pure and Applied Geophysics

Structural Properties of the San Jacinto Fault Zone at Blackburn Saddle from Seismic Data of a Dense Linear Array

Pieter-Ewald Share,[1] Amir A. Allam,[2] Yehuda Ben-Zion,[1] Fan-Chi Lin,[2] and Frank L. Vernon[3]

Abstract—We image the San Jacinto fault zone at Blackburn Saddle using earthquake waveforms recorded by a ~ 2-km across-fault linear array with 108 three-component sensors separated by ~ 10–30 m. The length and spatiotemporal sampling of the array allow us to derive high-resolution information on the internal fault zone structure with spatial extent that can be merged with regional tomography models. Across-fault variations in polarization, amplitude, and arrival time of teleseismic *P* waves indicate abrupt changes in subsurface structure near the surface trace of the fault (sensor BS55) and ~ 270 m to the northeast (sensor BS34). Analysis of fault zone head waves from local events reveals the existence of a deep bimaterial interface that extends from the array to at least 50 km southeast and has a section with > 10% velocity contrast. This analysis also corroborates the teleseismic results and indicates a broad damage zone primarily northeast of the fault bounded by a shallow bimaterial interface near BS34 that merges with the deep interface. Detection and waveform inversions of Love-type fault zone trapped waves generated by local events indicate a trapping structure within the broader damage zone with width of ~ 150 m, velocity reduction of ~ 55% from the surrounding rock and depth extent of ~ 2 km. The performed analyses provide consistent results on the subsurface location of the main seismogenic fault and properties of a major bimaterial interface and damage structure. The imaged fault zone properties are consistent with preferred propagation direction of earthquake ruptures in the area to the northwest.

Key words: Earthquake dynamics, San Jacinto fault zone, high-resolution imaging, seismic array, body waves, interface waves, guided waves.

1. Introduction

Clarifying the internal velocity structure of fault zones is important for many seismological and fault mechanics studies. A velocity contrast across a fault can affect the directivity, velocity and crack versus pulse style of earthquake ruptures (e.g., Weertman 1980; Andrews and Ben-Zion 1997; Shlomai and Fineberg 2016), as well as derived earthquake locations and focal mechanisms (e.g., Oppenheimer et al. 1988; McGuire and Ben-Zion 2005). Properties of the core damage zone around the fault contain information on processes and stress conditions operating during earthquake ruptures (e.g., Sibson 1989; Xu et al. 2012). Asymmetric damage zone with respect to the main fault may indicate a preferred directivity of large earthquake ruptures on that fault section (e.g., Ben-Zion and Shi 2005; Dor et al. 2006; DeDontney et al. 2011). Along-strike (dis)continuity of bimaterial fault interfaces can be relevant for the likely extent of earthquake ruptures (e.g., Dor et al. 2008; Share and Ben-Zion 2016).

A set of seismic arrays that cross the San Jacinto fault zone (SJFZ) in southern California at various locations (Fig. 1a) provides unique opportunities for detailed imaging of bimaterial fault interfaces and damage zones, in relation to geological (e.g., Sharp 1967; Rockwell et al. 2015) and regional tomographic (e.g., Allam and Ben-Zion 2012; Barak et al. 2015; Fang et al. 2016) results. Previous studies analyzed data recorded by different linear arrays with apertures of ~ 200–450 m (e.g., Yang et al. 2014; Qiu et al. 2017) at various locations, and a dense rectangular array with a linear dimension of ~ 600 m (Ben-Zion et al. 2015; Hillers et al. 2016; Qin et al. 2018) at the SGB site. In particular, Share et al.

Electronic supplementary material The online version of this article (https://doi.org/10.1007/s00024-018-1988-5) contains supplementary material, which is available to authorized users.

[1] Department of Earth Sciences, University of Southern California, Los Angeles, CA 90089, USA. E-mail: pshare@usc.edu
[2] Department of Geology and Geophysics, The University of Utah, Salt Lake City, UT 84112, USA.
[3] Scripps Institution of Oceanography, University of California San Diego, La Jolla, CA 92093, USA.

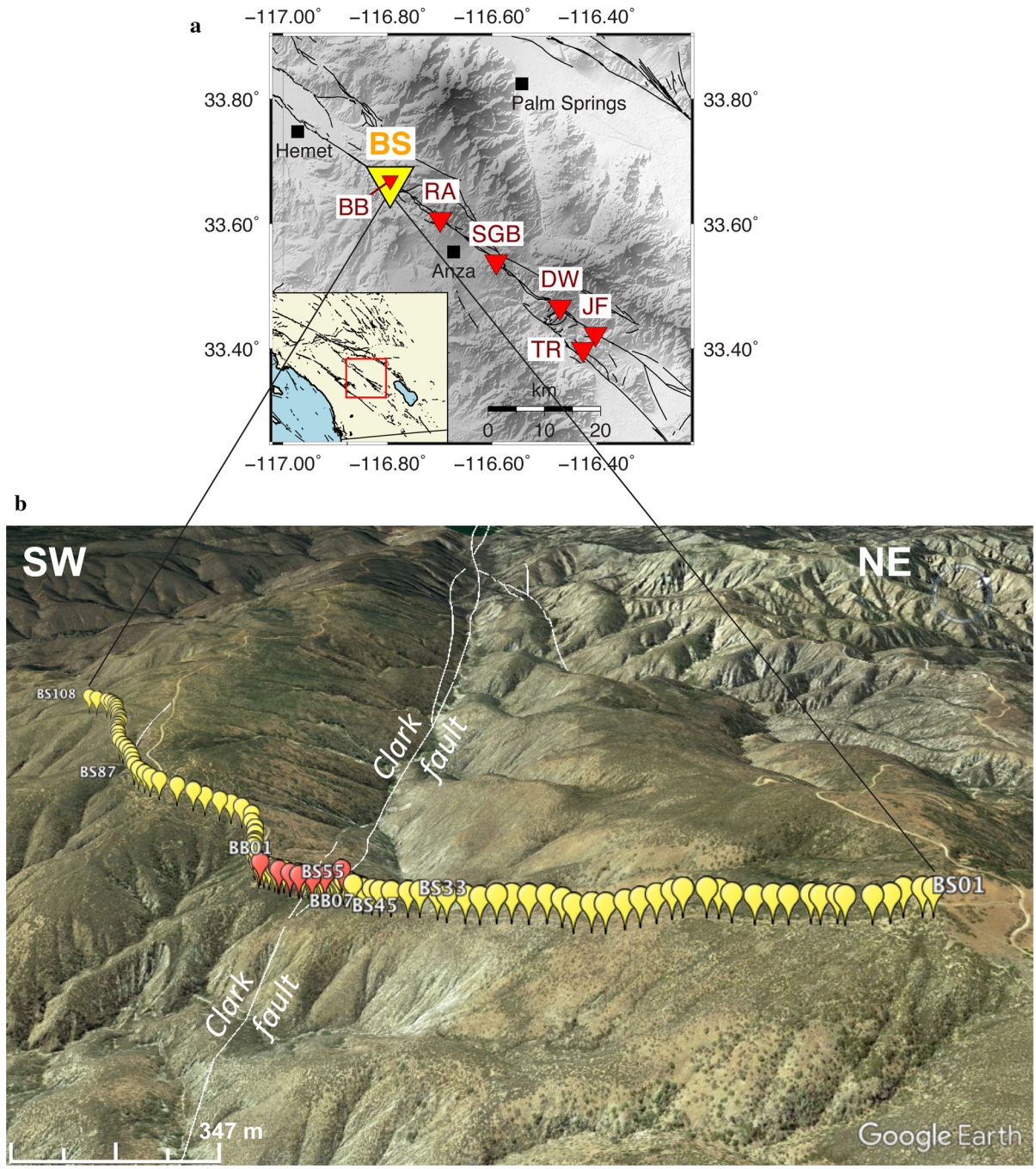

Figure 1
Dense linear arrays along the San Jacinto fault zone (SJFZ). **a** Locations of the Blackburn Saddle array analyzed in the present study (BS, large yellow triangle) and other arrays (BB, RA, SGB, DW, JF and TR, small red triangles) installed along the SJFZ. The towns of Hemet, Anza and Palm Springs (black squares) are shown for reference. **b** 108 nodes of the BS array (yellow icons) crossing the Clark fault (CF) surface trace. For reference, locations of the 7 BB stations are also shown (red icons)

(2017) analyzed data from local earthquakes and teleseismic events recorded by the BB linear array across the Clark branch (CF) of the SJFZ at Blackburn Saddle northwest of Anza, consisting of 7 sensors with ∼ 200-m aperture. The site ruptured during two large earthquakes in the last 250 years,

the M 7.2–7.5, 1800 (Salisbury et al. 2012) and the M 6.8, 1918 (Sanders and Kanamori 1984) events. The results indicated the presence of a $>$ 100-m-wide asymmetric damage zone (most damage on northeast side of the CF), which terminates at a local bimaterial interface northeast of the array that is connected to a regional bimaterial interface at depth. Due to the short aperture of the array, the spatial extent of the damage zone, which can be wider than 1 km (e.g., Cochran et al. 2009), was not well constrained. Also, the location of the bimaterial interface at the surface was not observed but inferred from comparison with data recorded by stations of the regional seismic network.

To provide more complete information on the inner structure of the SJFZ at Blackburn Saddle over a much larger area, a new array (BS) extending $\sim$ 1 km on each side of the CF was deployed in late 2015. The BS array had 108 densely spaced 3-component Zland nodes covering and extending well beyond the locations of the previous short BB array (Fig. 1b). In the present study, we analyze data recorded by this first-of-its-kind 3-component nodal array to derive a high-resolution structural model of the fault zone over a spatial extent that can be merged with the tomographic images in the region. The analyzed data include P and S waveforms generated by local earthquakes and P waveforms of teleseismic events. The employed seismic phases are sensitive to bimaterial interfaces, damage zone structure and the surrounding rocks, and can better be distinguished and analyzed using the large-aperture BS array spanning all these structures. Variations in teleseismic arrivals are used to determine large-scale structural changes across the fault zone including the extent of a broad damage zone at the site. Local arrivals are analyzed for the presence of waveform changes across the fault, fault zone head waves (FZHW) and fault zone trapped waves (FZTW). The fault zone phases are used to image properties of the fault bimaterial interface and the core inner damage zone that acts as a seismic trapping structure.

In the next section, we provide more details on the array stations and data. The analysis techniques and results are described in Sects. 3 and 4. Section 3 examines spatial variations of polarizations, amplitudes and delay times of teleseismic data across the array. Section 4 includes analysis of waveform changes across the array and analyses of FZHW and FZTW based on local earthquake waveforms. The results are summarized and discussed in relation to other studies of fault zones and earthquake physics in the final Sect. 5.

2. *Instrumentation and Data*

The BS array comprises 108 three-component 5-Hz geophones installed along an approximately fault-perpendicular line crossing the CF surface trace with 26 instruments placed off the main line. The array recorded data continuously at 1000 Hz sampling starting on 21 November 2015 for 35 days. Station BS55 was nearest to the CF trace and stations BS1 and BS108 were at the northeastern and southwestern ends, respectively (Fig. 1b). Along the line, stations were 10 m apart in a 400-m-wide zone centered on the surface trace and spaced $\sim$ 30 m to the northeast and southwest of that zone. Only data from stations BS1 to BS108 were used in this study given our focus on across-fault structural variations. The instrument response was not removed from the waveforms as Zland nodes reliably record phases from $\sim$ 0.1 Hz to well above local P wave bandwidth (Ringler et al. 2018). The slight reduction in amplitude of lower frequency teleseismic arrivals introduced by the instrument response does not influence our analysis results in Sect. 3, because we are interested in relative changes in waveform across the array and this amplitude reduction is equal for all stations.

The earthquake catalog of the Southern California Earthquake Data Center (SCEDC 2013) was used to extract P waveforms for all $M > 5$ teleseismic earthquakes (within 30°–100°) deeper than 500 km that occurred during the installation period. Four earthquakes matched these criteria but two of them occurred within 60 km and 5 min of each other, so the second of these was not considered. Waveforms for the 3 remaining events (Fig. 2a; Table 1) were extracted from continuous BS recordings using the P wave arrival time at the BS55 location at sea level predicted with TauP (Crotwell et al. 1999). After extraction, the mean and trend were removed and a

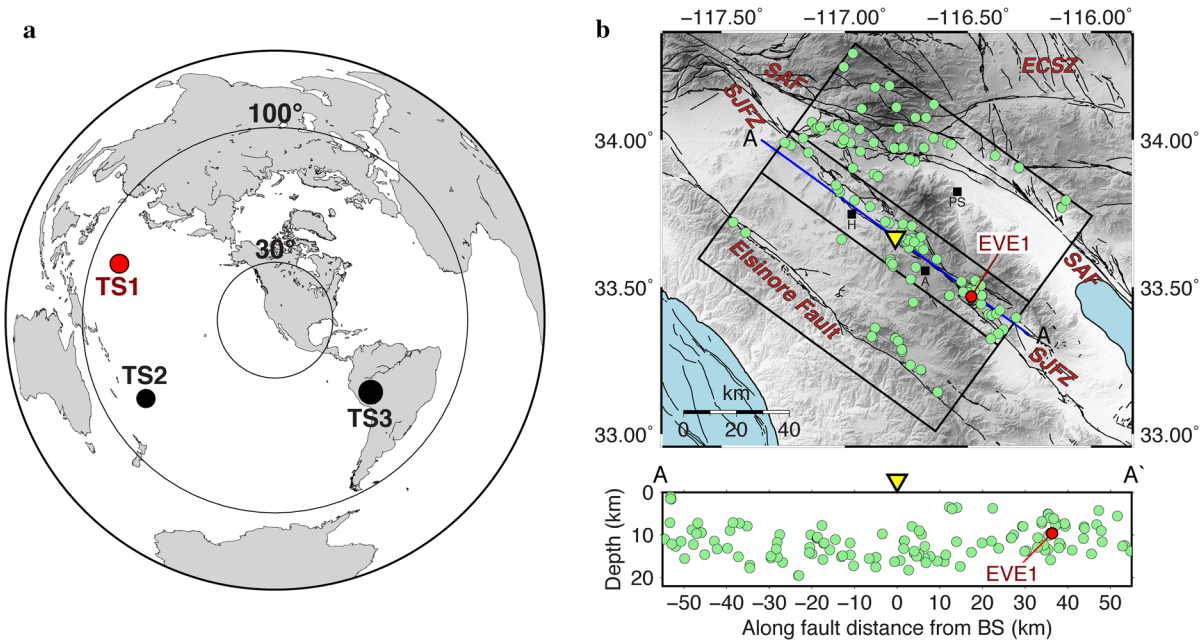

Figure 2

Data employed in the present study. **a** Locations of the 3 $M > 5$ teleseismic earthquakes used (TS1-TS3). Results of data analysis from an example event (TS1) are shown in Fig. 3. Waveforms from events TS2 and TS3 are given in Fig. S1. **b** Locations of $M_W > 1$ earthquakes (143 in total, circles) within a 110 km by 100 km region (big black box) centered on the BS array (yellow triangle) and aligned with the CF surface trace. The small black rectangle highlights earthquakes within 10 km of the CF. Waveforms from an example event (EVE1, red circle) are shown in Fig. 5a. H = Hemet; A = Anza; PS = Palm Springs; SAF = San Andreas fault; ECSZ = Eastern California Shear Zone. A depth section of events projected along the profile A–A′ is plotted at the bottom

low-pass Butterworth filter with corner frequency 2 Hz was applied.

The Hauksson et al. (2012) relocated catalog for Southern California (extended to later years) was used to extract waveforms from local events. In total, 143 $M_W > 1$ earthquakes located within a 110 km by 100 km box centered on the BS array and aligned with the CF trace occurred during the installation period (Fig. 2b). For these events, we used waveforms 5 s before and 30 s after the origin times reported in the catalog. A band-pass Butterworth filter between 2 and 20 Hz was applied to these waveforms after the initial removal of any trend from the data. As illustrated in Fig. 3a and later plots of waveforms, the long BS array provides a far better coverage of the fault zone than the previously analyzed data recorded by the short BB array.

3. Teleseismic Earthquake Analyses

The early *P* waves from teleseismic events are analyzed for changes in polarization, amplitude and arrival times. Polarization and amplitude will change in response to topographic and structural changes that have length scales comparable to the long

Table 1

Catalog of the teleseismic earthquakes analyzed

Event	SCEDC ID	Origin time UTC	Latitude	Longitude	Depth (km)	Magnitude
TS1	37268101	2015/11/24, 13:21:35.800	18.7906	145.3115	586.20	6.00
TS2	37268269	2015/12/06, 17:09:28.800	− 18.1903	− 178.6798	544.30	5.80
TS3	37268157	2015/11/24, 22:45:38.000	− 10.5484	− 70.9038	600.60	7.60

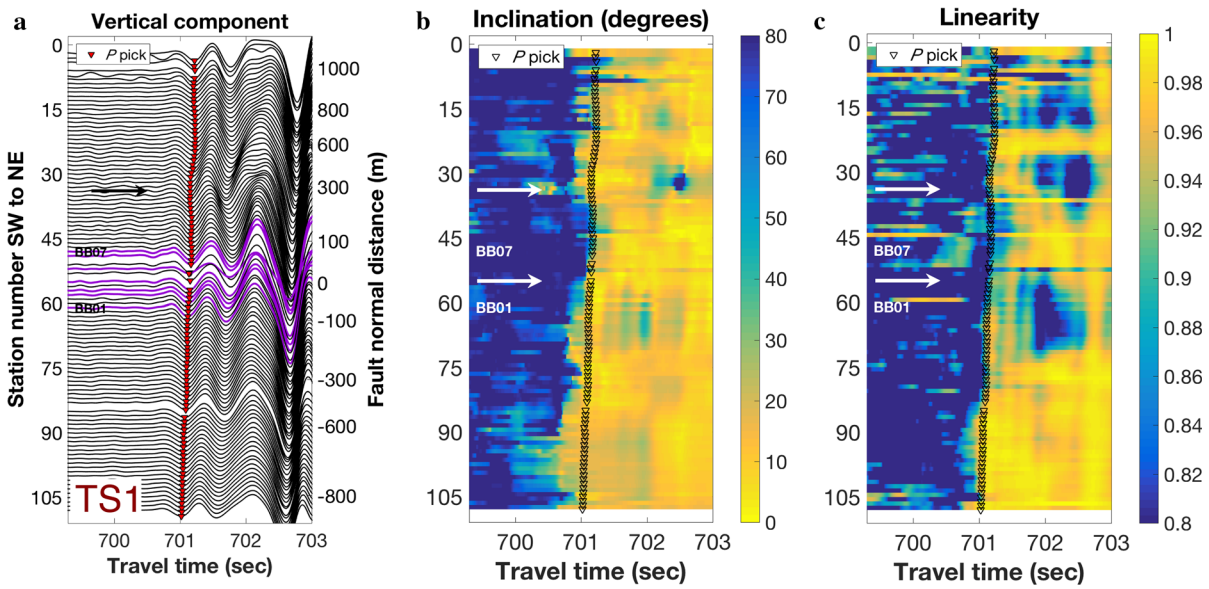

Figure 3
Analysis of waveforms recorded by the BS array from an example teleseismic event. **a** Early *P* waveforms (velocity seismograms) generated by event TS1. All seismograms are normalized by the same value. Noisy traces are removed. Red triangles denote manual *P* picks and the black arrow points to an abrupt change in waveform character across traces recorded near BS34. Waveforms recorded near BB array locations are colored purple with the southwestern most and northeastern most ones denoted by BB01 and BB07. **b**, **c** Inclination of the largest eigenvector and linearity calculated using a 0.75 s window. White arrows highlight abrupt changes in these parameters

wavelengths (> 1 km) of the teleseismic energy (Jepsen and Kennett 1990; Neuberg and Pointer 2000). Arrival times corrected for variations due to different propagation paths can be used to determine slowness changes at similar large length scales (e.g., Schmandt and Clayton 2013; Qiu et al. 2017). Here, such analyses are done to identify large-scale vertical (or near vertical) fault interfaces and regions of increased slowness potentially corresponding to fault damage zones.

3.1. Polarization and Amplitude Variations

For each of the 3 teleseismic events, we use the vertical component to manually pick the first coherent peaks (positive or negative) across the array and designate them *P* arrivals (*P* picks in Fig. 3a). We then visually inspect the waveforms 2 s after these picks for abrupt changes in character. As an example, for event TS1 (location in Fig. 2a), most rapid changes in arrival time and waveform are observed around station BS34 (270 m northeast of the CF trace, Fig. 3a). Similar changes in arrival time and waveform are found near the same station for the other 2 events (Fig. S1). A sharp change in arrival time and waveform character occurs near station BS55 (location of CF trace) for event TS3 (Fig. S1b).

Next, we apply polarization analysis (Jurkevics 1988) to all three components to quantify waveform changes recorded across the array. The analysis employs a moving time window of length 0.75 s (750 samples). For each window, the three components are combined in a 750×3 matrix and the covariance of that matrix is computed. The eigenvalues (λ_1, λ_2, λ_3) and eigenvectors ($\boldsymbol{u}_1$, $\boldsymbol{u}_2$, $\boldsymbol{u}_3$) of the covariance matrix give, respectively, the amplitudes and directions of the axes of the polarization ellipse. The largest eigenvalue λ_1 corresponds to the amplitude of maximum polarization with direction $\boldsymbol{u}_1$. For a *P* wave, direction $\boldsymbol{u}_1$ gives the inclination angle as

$$\mathrm{Inc} = \cos^{-1}(u_{11}). \tag{1}$$

From the eigenvalues, the degree of polarization/linearity can be calculated using

$$q = 1 - ((\lambda_2 + \lambda_3)/2\lambda_1), \tag{2}$$

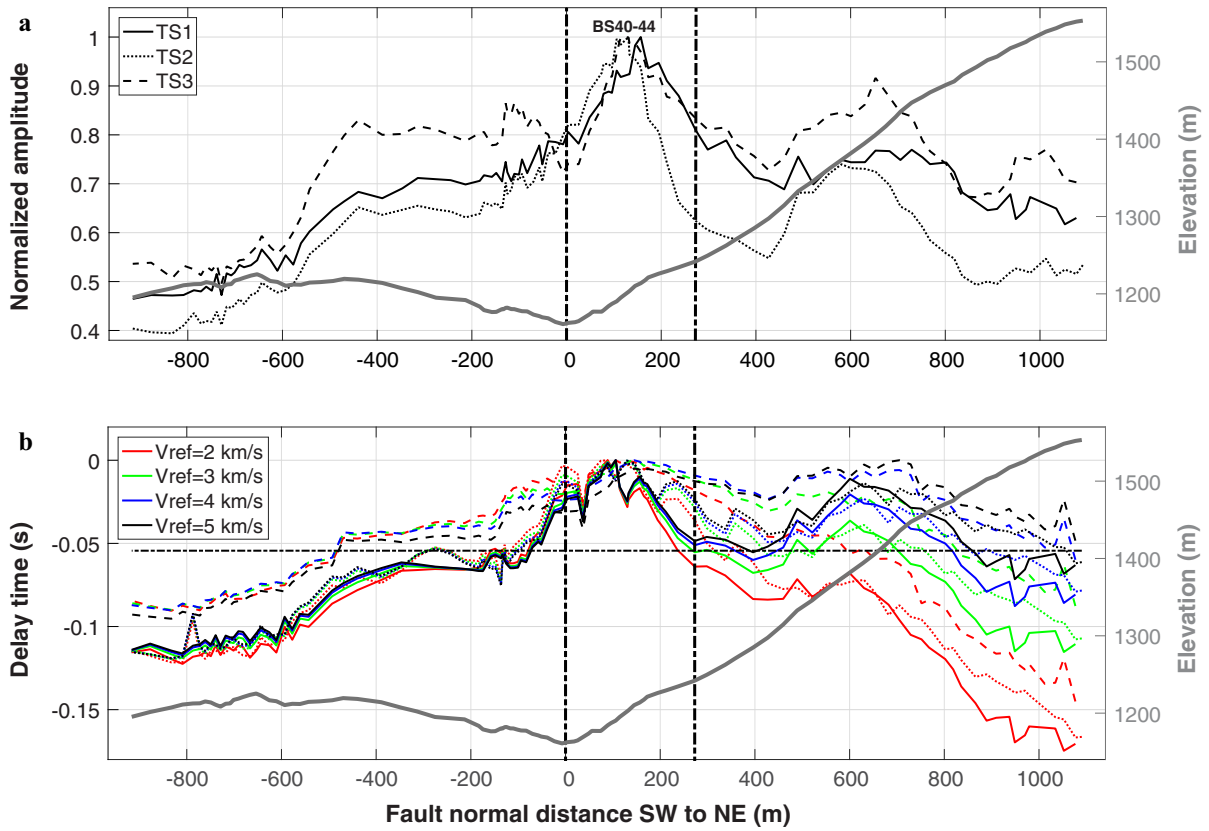

Figure 4
Amplitude and arrival time variations of teleseismic *P* waves across the array. **a** Maximum amplitudes within 1.5 s windows starting at the *P* picks for the 3 events (TS1—solid line; TS2—dotted line; TS3—dashed line, information in Table 1). Vertical black dot-dashed lines represent the locations of stations BS55 (left) and BS34 (right) and the horizontal black dot-dashed line depicts the median of the delay times shown. Gray line depicts changes in topography across the array. **b** Delay times for 3 events (same line styles as in **a**) and reference velocities of 2 km/s (red), 3 km/s (green), 4 km/s (blue) and 5 km/s (black) used during correction for topography

with q being 1 when the P wave is linearly polarized and 0 for perfectly uncorrelated motion. The inclination and linearity are calculated for each 0.75-s window using Eqs. (1) and (2) and are assigned to the time of the final sample in the moving window (time windows are trailing). Application to the example event TS1 indicates large changes in inclination (± 30°, Fig. 3b) and linearity (± 0.1, Fig. 3c) around station BS34. Large changes in inclination and linearity are also observed near BS55. Similar changes in inclination and linearity are detected at BS34 and BS55 for the other 2 events. Less prominent changes in inclination and linearity across the array (for example near BS20 and BS80) correspond to smaller scale structures in the area that are left unresolved.

The changes in arrival time and waveform character near BS34 correspond to lateral variations in large-scale subsurface structure rather than sudden changes in topography, since similar topographic gradient exists for stations BS1–55 (Fig. 4). The abrupt waveform change near station BS55 is correlated with the mapped surface trace of the CF at the site (Sharp 1967; Rockwell et al. 2015). Figure 4a displays the maximum amplitude within a 1.5-s window starting at each P pick for the 3 teleseismic events. A 1.5-s window is approximately equal to the largest period observed for the early P waves. The results show that stations BS40–44 (110–150 m northeast of the CF trace) consistently record the largest amplitude ground motion. The amplified motion may be caused by a core fault damage zone

beneath stations BS40–44 (e.g., Ben-Zion and Aki 1990; Lewis et al. 2005). The smaller scale changes in the results of this section are likely related to secondary lateral variations of the fault zone structure and topography.

3.2. Delay Time Analysis

To focus on changes associated with the fault zone structure, arrival times are corrected in two steps. For a given event, the travel times from source to stations without taking elevation into account are predicted. Following this, travel times from sea level to the surface are computed using a homogeneous reference velocity. The total predicted arrival times are then subtracted from the picked times and the residual variations (delay times) between stations are used to infer subsurface slowness. Stations with larger delay after correction overlie regions of greater slowness.

Arrival times at sea level for different stations are approximated using TauP and a 1D velocity model that is a combination of the IASP91 model for the mantle (Kennett 1991) and the model of Hadley and Kanamori (1977) for the crust. Travel times from sea level to the surface are calculated using the ray parameter for each event obtained from TauP and reference velocities of 2 km/s, 3 km/s, 4 km/s and 5 km/s (Fig. 4b). After subtracting the calculated times from the picked times, each resulting delay time profile is normalized by subtracting the current maximum delay. This allows comparisons of profiles for different events and reference velocities. There is generally good agreement among the normalized profiles, although the large topographic gradient northeast of the CF produces a spread in delay time profiles for the different reference velocity corrections (Fig. 4b). Irrespective of the spread between the curves, maximum delay times are consistently observed for stations BS41–47 (90–140 m northeast of the CF trace). This suggests greater slowness beneath these stations, which agrees overall with the maximum amplitudes plotted in Fig. 4a and subsequent analysis of FZHW and FZTW in Sects. 4.2 and 4.3. Less prominent maxima in amplitude and delay time curves (for example 600–700 m northeast of CF trace, Fig. 4) again suggest minor damage structures or other heterogeneities. These features should be considered as potential targets for future geological/geophysical studies around the Blackburn Saddle site.

4. Local Earthquake Analyses

4.1. Waveform Visual Inspection

We perform a similar visual inspection of waveforms from local events for evidence of lateral changes in the subsurface structure beneath the array. The shorter wavelengths (higher frequencies) of local arrivals allow observation of large-scale variations across the fault at higher resolution compared to teleseismic arrivals.

Waveforms from local earthquakes (Fig. 2b) are first processed with an automatic algorithm (Ross and Ben-Zion 2014; Ross et al. 2016) to identify the onset times of P and S waves. We then visually inspect early P and S waves 0.5 s after these automatic picks for anomalous changes in character. Figure 5a shows vertical component waveforms from an example event EVE1 (location in Fig. 2b) and associated P and S picks. The P waveforms recorded southwest of station BS34 show a 4–5 factor increase in maximum amplitude compared to P waveforms recorded northeast of BS34. Similar to Sect. 3.1, this abrupt change in waveform character implies a lateral change in subsurface structure near BS34. Moreover, P peak amplitudes recorded southwest of BS34 are associated with phases (right orange line in Fig. 5b) arriving $\sim$ 0.2 s after the P first arrivals (left orange line in Fig. 5b). The P first arrivals recorded at these stations are potential FZHW, while the trailing large amplitude phases are direct P waves. This suggests that the structural change near BS34 is associated with a bimaterial interface. Following the S arrivals, stations BS41–45 record an anomalous large amplitude wave packet (orange box in Fig. 5c). These are potential FZTW associated with the core damage zone along the CF through Blackburn Saddle. Similar FZHW and FZTW are observed in waveforms from several other events and we analyze them in greater detail below.

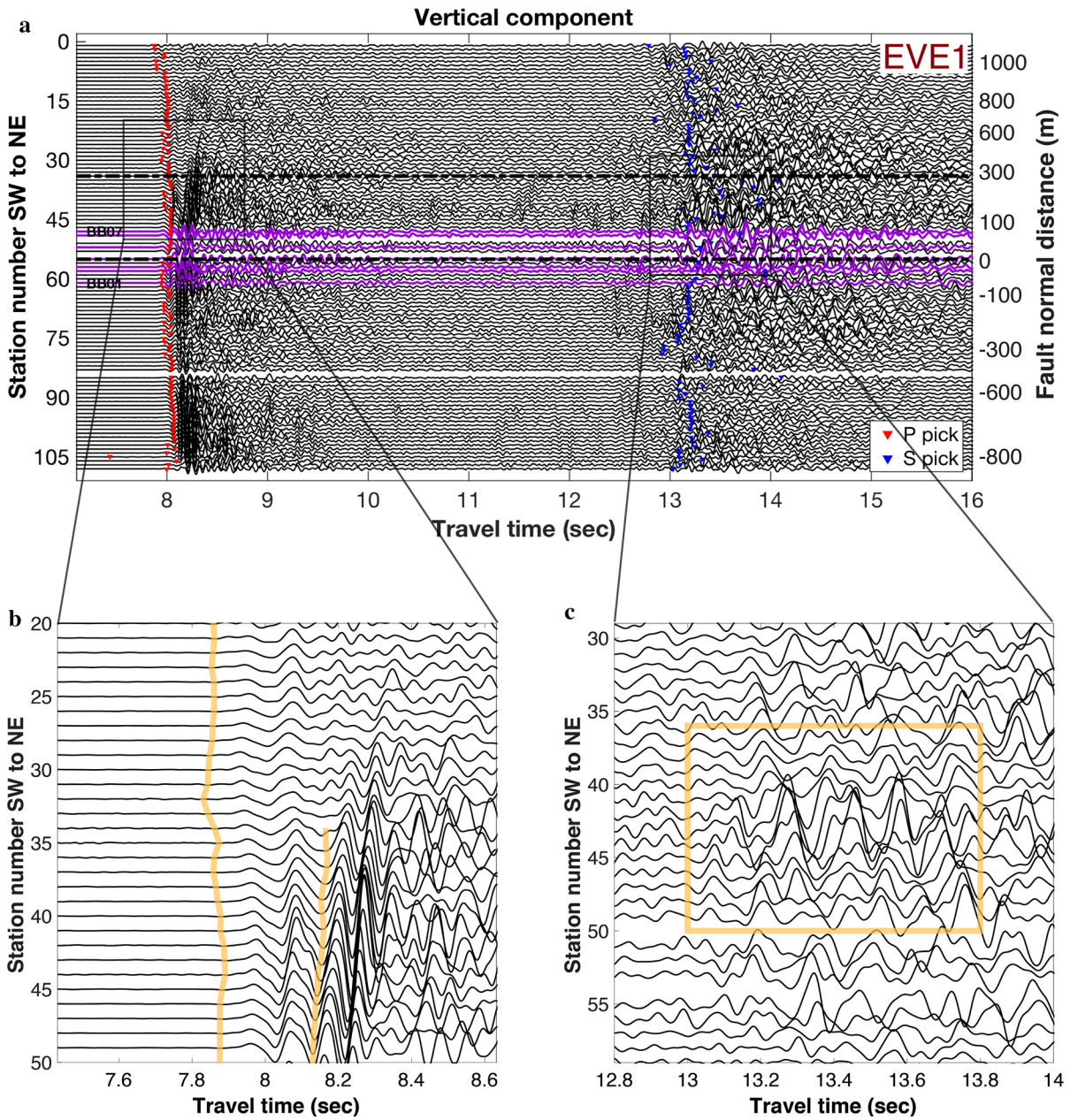

Figure 5
Waveforms (velocity seismograms) generated by local event EVE1 (M_W 1.9). **a** Waveforms recorded across the array with automatic *P* (red triangles) and *S* (blue triangles) picks highlighting the arrivals of these respective phases. All seismograms are normalized by the same value. Noisy traces are removed. The black dot-dashed lines show locations of the CF trace (bottom line) and another large-scale structure to the northeast of the CF (top line, see Sect. 3.1). Waveforms recorded near BB array locations are colored purple with the southwestern most and northeastern most ones denoted by BB01 and BB07. **b** Zoom in of early *P* arrivals at stations BS20–50. The leftmost orange line represents manually picked *P* first arrivals across these stations whereas the orange line to the right of it indicates the later arrival of large amplitude *P* phases at stations southwest of $\sim$ BS34 only. **c** Zoom in of *S* arrivals at stations BS29–59. The orange square highlights an anomalous large amplitude wave packet recorded at stations BS41–45

4.2. Fault Zone Head Waves

4.2.1 Methodology

FZHW are critically refracted emergent phases that travel along a fault bimaterial interface with the velocity of the faster medium (Ben-Zion 1989). They arrive at stations in the slower medium before the impulsive direct P waves and are observed up to a fault-normal critical distance x_c given by

$$x_c = r \cdot \tan\left(\cos^{-1}(\alpha_s/\alpha_f)\right), \quad (3)$$

where r, α_s and α_f denote the propagation distance along the fault (both along-strike and up-dip direction) and average P wave velocities of the slower and faster media, respectively. The differential time Δt between FZHW and direct P wave for a station near the fault is given by

$$\Delta t = r/\alpha_f \cdot \eta/(1-\eta), \quad (4)$$

where $\eta = (\alpha_f - \alpha_s)/\alpha_f$ is the fractional velocity contrast across the fault (Ben-Zion 1989; Qiu et al. 2017). Because FZHW radiate from the fault and direct P waves propagate from the epicenter, FZHW have horizontal particle motion with a significant fault-normal component (Bulut et al. 2012; Allam et al. 2014; Share and Ben-Zion 2016) compared to that of direct P waves. For on-fault events, the FZHW and trailing direct P waves on the slow side of the fault have opposite first motion polarities (Ben-Zion 1989; Ben-Zion and Aki 1990).

4.2.2 Results

We identify FZHW with an automatic detector (Ross and Ben-Zion 2014) in conjunction with visual inspection and analysis using the aforementioned criteria. The detector flags P waveforms with an emergent phase followed by an impulsive arrival with a time separation between a minimum value (0.065 s representing the width of a narrow P wave wiggle) and a maximum value that depends on hypocentral distance. As an example, a maximum time separation of 0.8 s is allowed over a distance of 40 km using the default parameters of the Ross and Ben-Zion (2014) algorithm. The detector is applied similarly to previous linear SJFZ array studies (Qiu et al. 2017; Share et al. 2017) using a slightly lower STA/LTA trigger threshold due to the lower SNR of BS array waveforms compared to the other arrays.

Focusing first on the 75 events within 10 km of the CF trace (Fig. 6a), which have magnitudes M_W 1–3, the automatic detector flags 316 potential FZHW for the 108 stations analyzed. The picked FZHW are from events located both northwest and southeast of the array (Fig. 6a). Though all stations have potential detections, those southwest of BS34 have more than double detections compared to stations northeast of BS34 (Fig. 6b). Some of the automatic picks are expected to be false (Ross and Ben-Zion 2014), and some may be associated with the edge of the damage zone (Najdahmadi et al. 2016) or a basin (Yang et al. 2015; Qiu et al. 2017), rather than a deep fault bimaterial interface that is the main imaging target here.

Based on visual inspection of the 75 events generating candidate FZHW, we find that events with epicenters near the CF surface trace within the trifurcation area (having large along-fault propagation distance) produce the clearest head waves. The locations of two example events HW1 and HW2 are shown in the inset of Fig. 6a. These events generate emergent (lower frequency, Fig. S2a) low amplitude first P arrivals (candidate FZHW) at stations southwest of BS34 (Fig. 7a, 1st and 2nd row), followed by larger amplitude impulsive arrivals (direct P waves) 0.1–0.3 s later. The differential time between the identified FZHW and direct P arrivals is largest near BS34 and decreases towards BS108 in the southwest (Eq. 3). Only impulsive P arrivals are recorded at stations northeast of BS34. These observations imply that a bimaterial interface is present below the surface location of station BS34.

The candidate FZHW and trailing direct P waves from near-fault events are substantiated by comparing their move-outs across the array with those of nearby reference events that do not produce FZHW propagating at depth. In the presence of a bimaterial fault, a reference event located sufficiently far off-fault in the slower medium produces a first arriving direct P wavefront at locations on the slow side with azimuth pointing to the epicenter. In contrast, direct P waves from a fast side reference event and FZHW from an event near the interface are refracted along the fault; so their arrivals on the slow side have

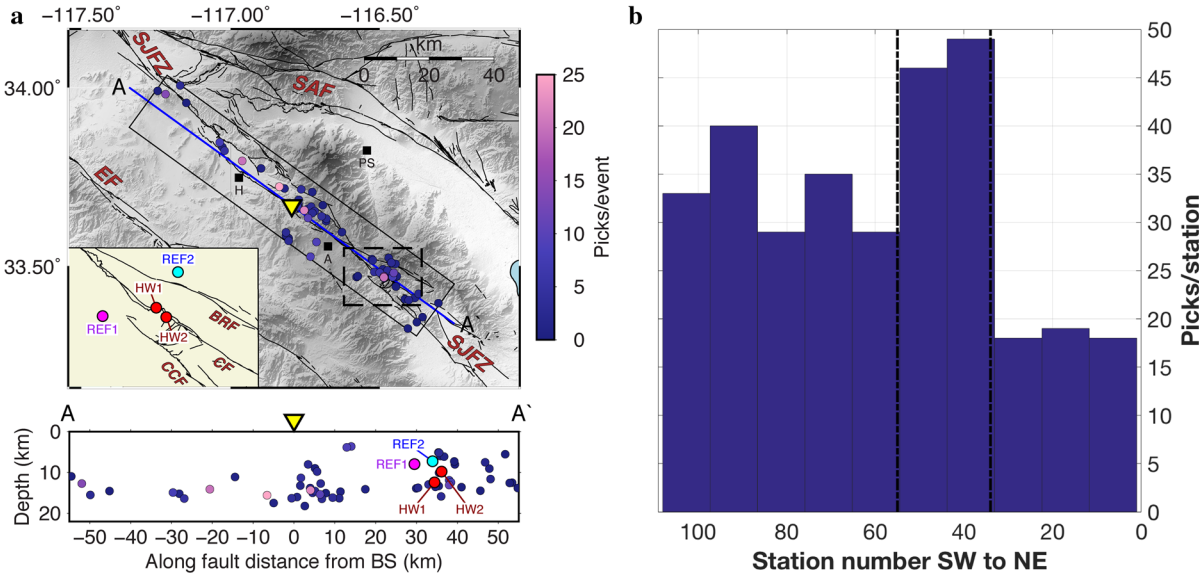

Figure 6

Identifying FZHW using an automatic detection algorithm. **a** Locations of events analyzed (circles inside solid black rectangle). Circle colors correspond to the number of stations with FZHW detections (blue = no detections, pink = most detections). The inset shows a zoom in of selected events located within the trifurcation area (dashed black box). FZHW are confirmed for events HW1 and HW2 near the CF (large red circles) using automatic detection and visual inspection (Fig. 7, 1st and 2nd rows). Reference events near the Coyote Creek (CCF) (REF1, magenta circle) and Buck Ridge (BRF) (REF2, cyan circle) faults that do not generate FZHW (Fig. 7, 3rd and 4th rows). A depth section of events projected along the profile A-A' is plotted at the bottom. **b** Histogram of number of FZHW detections per station for events in **a**. Dot-dashed lines represent the locations of stations BS55 (left) and BS34 (right)

azimuth with a larger fault-normal component compared to the source-receiver azimuth. If the fast side reference event is relatively close to a near-fault event, the move-out of the wavefront across locations on the slow side from the former will be similar to that of critically refracted FZHW generated by the latter. Likewise, move-outs of direct *P* wavefronts from slow side reference and near-fault events will be similar. We, therefore, identify FZHW and trailing direct *P* waves as arrivals with most similar move-outs to that of first *P* arrivals from fast side and slow side reference events, respectively. Comparing move-outs of reference and near-fault events in this manner to distinguish FZHW and direct *P* waves in a structurally complex fault zone with variable focal mechanisms is more robust (Najdahmadi et al. 2016; Share et al. 2017) than applying horizontal polarization analysis. The latter is useful primarily for simple faults and strike-slip mechanisms (e.g., Bulut et al. 2012; Allam et al. 2014; Li and Peng 2016).

We choose events near the Coyote Creek (REF1, Figs. 6a, inset, 7a, 3rd row) and Buck Ridge (REF2, Figs. 6a, inset, 7a, 4th row) faults as reference events on nominally slow and fast sides of the CF, respectively (Allam and Ben-Zion 2012). First arrival *P* waves from the reference events are impulsive and large in amplitude at all stations (Fig. S2b). Compared to REF1 (magenta line in Fig. 7a, 3rd row), REF2 has *P* arrival times that increase more with fault-normal distance from BS34 towards stations in the southwest (cyan line in Fig. 7a, 4th row). This implies that the wavefront from REF2 has the azimuth with larger fault-normal component on the nominally slow side of the fault. FZHW move-outs across stations southwest of BS34 from events HW1 and HW2 are highly correlated with the move-out of *P* arrivals from REF2 (cyan lines Fig. 7a, 1st and 2nd rows). At the same stations, direct *P* wave move-outs from events HW1 and HW2 are approximately equal to the move-out observed for REF1 (magenta lines Fig. 7a, 1st and 2nd rows). These comparisons show that the observed FZHW and direct *P* waves are radiated from the fault and the source, respectively. In addition, the comparisons reveal that the

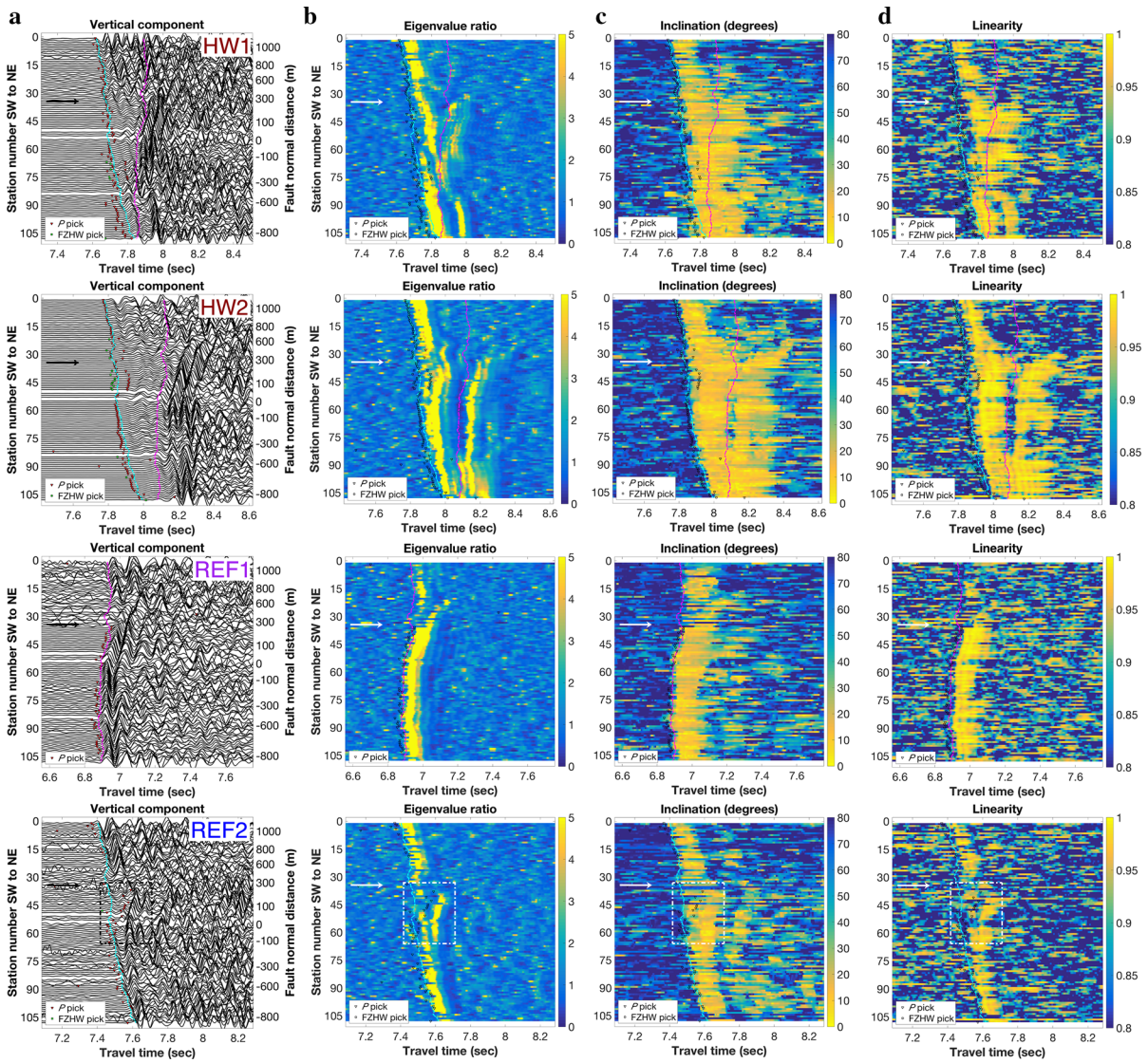

Figure 7

Observed waveforms and polarization analysis of FZHW. **a** *P* waveforms (velocity seismograms) generated by events HW1 (1st row), HW2 (2nd row), REF1 (3rd row) and REF2 (4th row). Seismograms are self-normalized and noisy traces are removed. Green squares and red triangles depict automatic FZHW and *P* picks, respectively. Waveforms recorded at locations southwest of BS34 (black arrows) from HW1 and HW2 contain FZHW while waveforms from REF1 and REF2 do not. Magenta line in row 3 and cyan line in row 4 represent manual picks for *P* first arrivals from events REF1 and REF2, respectively. Cyan and magenta lines in rows 1 and 2 are the same as in rows 3 and 4 but shifted in time to align with the *P* first arrival (candidate FZHW) and onset of the impulsive direct *P* wave at station BS55, respectively. **b**–**d** The ratio of the largest eigenvalue between neighboring windows, inclination of the largest eigenvector and linearity calculated within the leading window for events HW1 (1st row), HW2 (2nd row), REF1 (3rd row) and REF2 (4th row). Symbols and lines have the same meaning as in **a**. Dot-dashed box in 4th row depict waveforms with candidate local FZHW (see text for details)

differential time Δt between FZHW and direct *P* wavefronts is larger for event HW2 compared to HW1 (colored lines are farther apart for HW2 versus HW1). This observation and Eq. (4) imply a continuous deep bimaterial interface associated with the CF, since HW2 is located farther from the array than HW1 (38 km versus 36 km).

Waveform characteristics of FZHW are quantified using polarization analysis as described in Sect. 3.1. Eigenvalues are computed using consecutive sliding

windows each 0.07 s long that overlap by 50%. In general, the largest eigenvalue of a window containing a FZHW will be larger than a signal containing only noise, and the largest eigenvalue corresponding to a direct *P* wave would be larger still (Allam et al. 2014; Share et al. 2017). For example, eigenvalue ratios computed between neighboring windows are $>$ 5 at all stations for first arrivals from events HW1 and HW2 (Fig. 7b, 1st and 2nd rows). Additionally, eigenvalue ratios > 5 are observed at stations southwest of BS34 upon later arrivals of direct *P* waves. Inclination of the largest eigenvector (Fig. 7c) and linearity (Fig. 7d) are also computed for the leading time window. First arrivals appear as coherent $< 15°$ anomalies in inclination that persist for 0.1–0.15 s at stations northeast of BS34 for events HW1 and HW2 (Fig. 7c, 1st and 2nd rows). For stations southwest of BS34 and same events, these anomalies persist for up to 0.3–0.4 s as they represent both FZHW and direct *P* waves. Coherent anomalies in linearity approximately equal to 1 similarly persist for longer times at stations southwest of BS34 (Fig. 7d, 1st and 2nd rows). Similar anomalous eigenvalue ratios, inclinations and linearity values are not observed for reference events REF1 and REF2 (Fig. 7b–d, 3rd and 4th rows). The polarization analysis indicates that FZHW have clear arrivals that stand out from the noise while the trailing direct *P* waves contain more energy than FZHW. The results are consistent with theoretical expectations (Ben-Zion 1989; Ben-Zion and Aki 1990) and previous observational studies. The analysis also shows, as expected, that both phases have near-vertical incidence and are linearly polarized.

Following the discussed analysis steps, 14 events near the trifurcation area generating clear FZHW propagating at depth are identified. In the case where events cluster, only one event per cluster is selected for further analysis. The selection process produces 5 events (Fig. 8a) with distinctly different hypocentral distances, and waveforms from these events are integrated to displacement prior to manual picking of FZHW and direct *P* arrivals. Using the picks and Eq. (4), we estimate the average velocity contrast across the CF between the BS array and generating events. FZHW picks are made on waveforms from stations southwest of BS34 where associated emergent phases begin to rise above the noise level (green

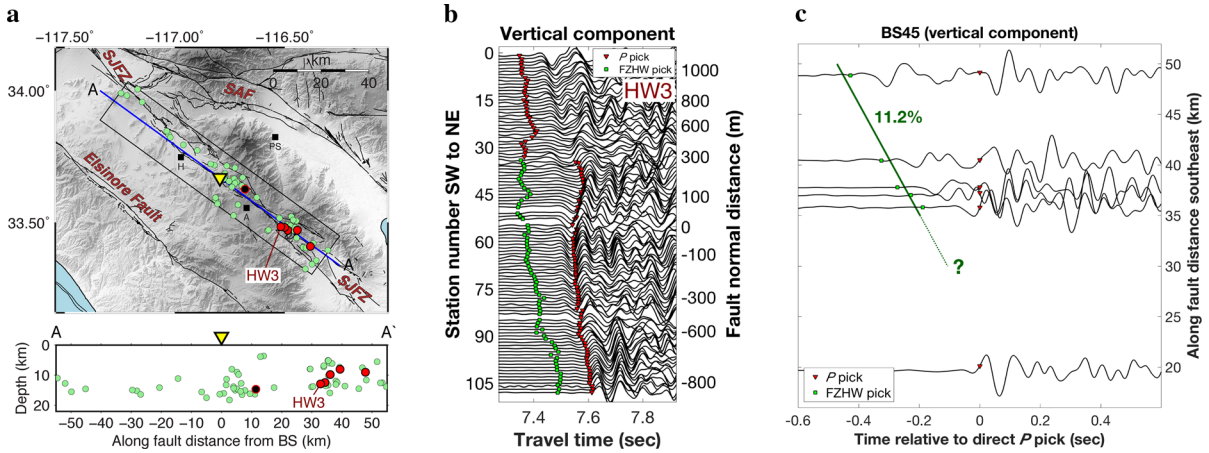

Figure 8

Average velocity contrast across the CF from FZHW move-out analysis. **a** Locations of 5 events (large red circles) used for the move-out analysis. The event closest to the array that generates FZHW is highlighted (HW3) and also shown is the location of an off-fault reference event (large red black-filled circle). A depth section of events projected along the profile A–A′ is plotted at the bottom. **b** *P* displacement seismograms from event HW3 and associated manual direct *P* (red triangles) and FZHW (green squares) picks (see text for picking procedure). Seismograms are self-normalized and noisy traces are removed. **c** Plot of displacement waveforms showing the linear move-out of FZHW (thick green solid line and squares) relative to direct *P* waves (red triangles) recorded at station BS45 for the 5 events in **a**. The move-out corresponds to a 11.2% average velocity contrast across that section of the CF. The thin green dotted line represents a speculative move-out in a region along the fault where there is no data (20–35 km). For comparison, the waveform from the reference event in **a** is also plotted at the bottom

squares in Fig. 8b). Direct P waves are picked (red triangles in Fig. 8b) using both a comparison of horizontal particle motion of early P waves from reference event REF1 and waveforms containing FZHW (similar to Share et al. 2017) and the move-out comparison discussed earlier using REF1 (Fig. 7). The obtained average velocity contrast over the along-fault distance section of 35–50 km from the array is 11.2% (thick green solid line in Fig. 8c). This estimate assumes an average α_f (Eq. 4) of 6.1 km/s based on the tomographic results of Allam and Ben-Zion (2012). The calculation is made using waveforms from representative station BS45 but using other stations leads to similar average velocity contrasts. From the event locations in Fig. 8a, the 11.2% velocity contrast corresponds to the trifurcation area and a depth section around 10 km. The average velocity contrast in the shallow crust is likely to be larger, since the velocity contrast typically decreases with depth (Ben-Zion et al. 1992; Lewis et al. 2007). In the distance range 20–35 km from the array we have no data, but it is clear that the average velocity contrast decreases closer to the array since the move-out (green) line in Fig. 8c has y-intercept significantly larger than 0. This is consistent with the earlier results of Share et al. (2017) who determined an average velocity contrast of $\sim$ 3% along the CF closer to the (short BB) array.

The analysis of near-fault events also shows evidence for local FZHW propagating exclusively along the edge of the fault damage zone (e.g., Li and Peng 2016; Najdahmadi et al. 2016). Stations located within the low-velocity damage zone (Figs. 4, 5c) have the most automatic detections (Fig. 6b) with some detections associated with events that do not generate FZHW propagating at depth. For example, event REF2 (Fig. 7, 4th row) does not generate FZHW traveling at depth, but stations BS34–65 record emergent P first arrivals followed by large amplitude impulsive arrivals $\sim$ 0.1 s later (dot-dashed rectangle in Fig. 7, 4th row). The emergent arrivals are potential local FZHW refracting along the contact between the damage zone and host rock (at the faster speed of the latter), while the trailing impulsive phases are direct P waves propagating within the damage zone.

To explore this further, we apply the automated head wave picker to the 68 events $>$ 10 km from the CF and combine the results of all events to search for local FZHW. Only near-fault events will generate FZHW propagating along a fault at depth. On the other hand, both near-fault and off-fault events can produce local FZHW since the waves from all events propagate through the damage zone before being recorded at surface stations above this zone. The automatic detector flags 357 potential local FZHW for the 68 off-fault events analyzed. As in Fig. 6b, stations within the damage zone have the most picks (Fig. 9a) that correspond to potential local FZHW. Stations northwest and southeast of the damage zone have similarly low numbers of detections (compare Figs. 6b and 9a), indicating (as expected) that none of the off-fault events generate FZHW propagating along the CF at depth.

Visual inspection and further analysis establish several clear examples of local FZHW at stations BS34–65 only. The locations of 15 such events and their respective waveforms recorded at representative stations within (BS43) and outside (BS25 and BS81) the damage zone are shown in Figs. 9b, c. The local FZHW are emergent phases (green line and squares) arriving before the direct P waves (red triangles) recorded at station BS43 (Fig. 9c, top). These phases are clearly not FZHW propagating along the CF at depth because an approximately constant Δt ($\sim$ 0.12 s) is observed with increasing hypocentral distance. If we assume that the local FZHW propagate near-vertically along the edge of the damage zone, Δt can be used to approximate the average P velocity contrast between damage zone and surrounding rock. Using Eq. (4), a depth extent of 2 km for the damage zone (see Sect. 4.3.2) and velocities of 2–5 km/s for the surrounding rock (similar to Sect. 3.2) give estimated velocity contrasts of $\sim$ 11–23%. This range is higher on average than the estimated contrast across the CF at depth as expected for a contrast between the damage zone and host rock.

4.3. Fault Zone Trapped Waves

4.3.1 Methodology

Spatially continuous low-velocity fault damage zones act as waveguides and generate constructive interference of S, P and noise phases that give rise to FZTW

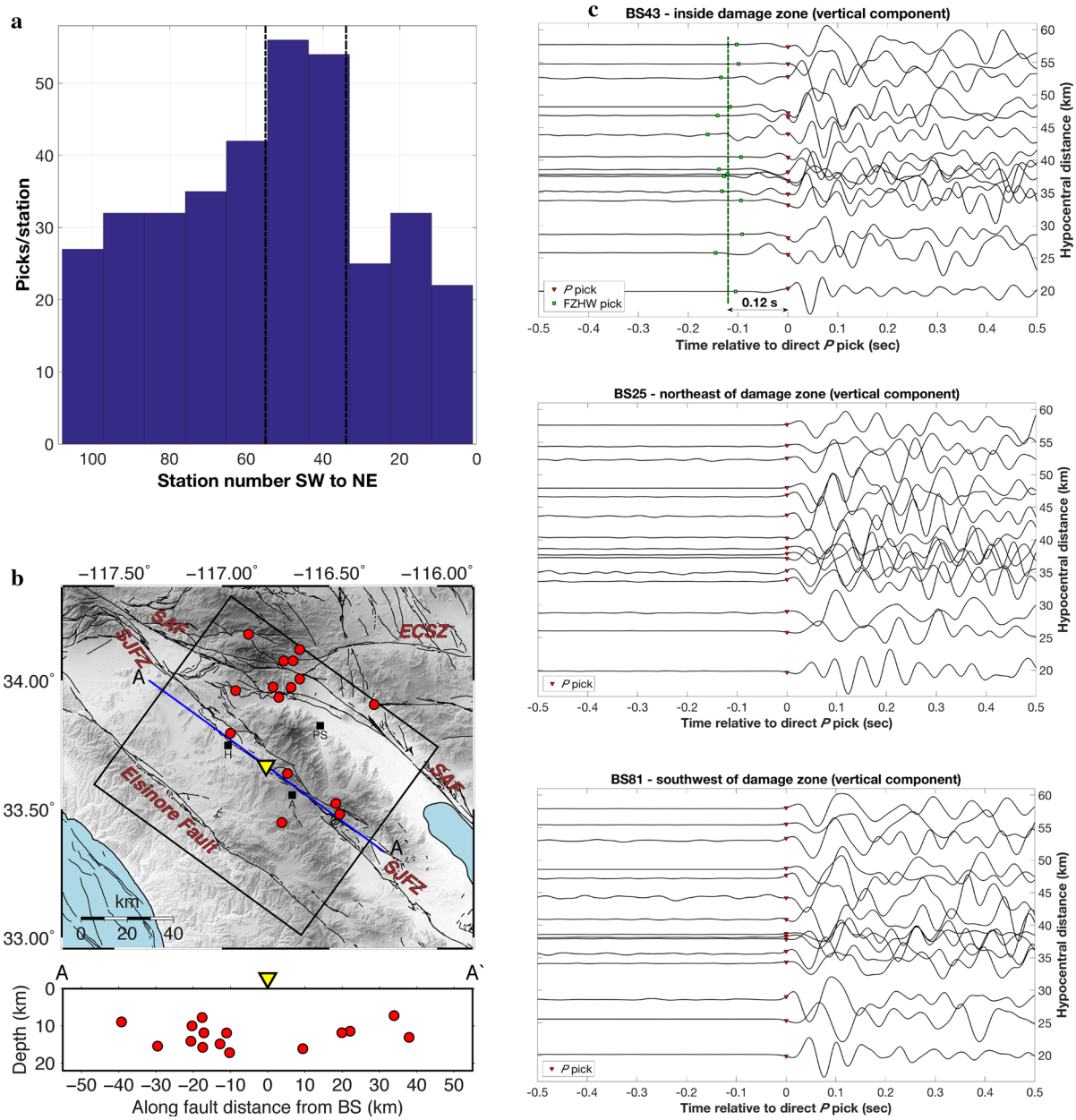

Figure 9

Analysis of local FZHW from off-fault events. **a** Histogram of number of FZHW detections per station for events > 10 km from CF (locations in Fig. 2b). Dot-dashed lines represent the locations of stations BS55 (left) and BS34 (right). **b** Locations of 15 example events (large red circles) that produce FZHW propagating exclusively along the damage zone edge. A depth section of events projected along the profile A–A′ is plotted at the bottom. **c** Self-normalized *P* velocity seismograms from events in **b** and recorded by stations within (BS43, top) and northeast (BS25, middle) and southwest (BS81, bottom) of the damage zone. Red triangles and green squares show manual direct *P* and local FZHW picks and the green line depicts the average early arrival time of the latter showing no apparent move-out

(e.g., Ben-Zion and Aki 1990; Hillers et al. 2014; Qin et al. 2018). These phases have been observed in various fault and geologic settings in California (Li et al. 1994; Lewis and Ben-Zion 2010) including the SJFZ using similar dense deployments (e.g., Qiu et al. 2017; Share et al. 2017) and elsewhere in the world

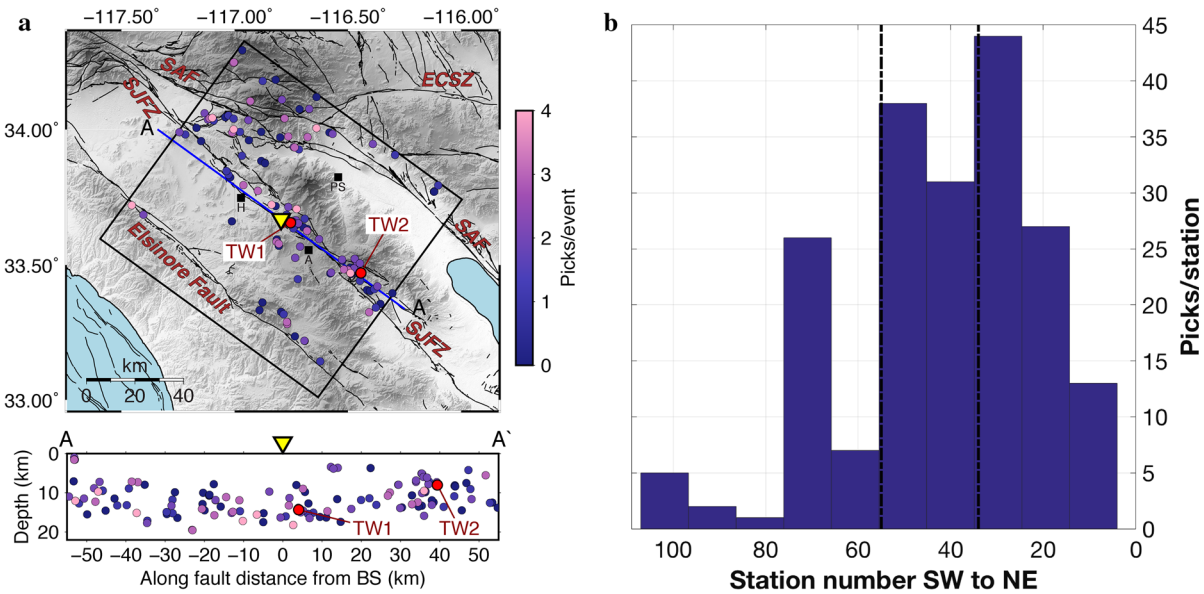

Figure 10

Identifying FZTW using an automatic detection algorithm. **a** Locations of the 143 events analyzed (circles inside black box). Circle colors correspond to the number of stations with FZTW detections (blue = no detections, pink = most detections). Waveforms from events TW1 (Fig. 11) and TW2 (Fig. S3) are inverted using a genetic algorithm approach to determine fault zone properties. A depth section of events projected along the profile A–A′ is plotted at the bottom. **b** Histogram of number of FZTW detections per station for events in **a**. Dot-dashed lines represent the locations of stations BS55 (left) and BS34 (right)

(e.g., Ben-Zion et al. 2003; Mizuno and Nishigami 2006; Eccles et al. 2015). FZTW appear on seismograms as high amplitude, long duration, anomalous frequency phases that follow direct arrivals and are observed only at stations that are within or near the trapping structure (e.g., Ben-Zion and Aki 1990; Li and Leary 1990; Lewis et al. 2005). Here, we focus on identifying and analyzing Love-type FZTW that follow the direct *S* wave (Ben-Zion 1998).

Similar to previous studies (Qiu et al. 2017; Share et al. 2017), we use an automated detection algorithm (Ross and Ben-Zion 2015) to flag candidate FZTW and visual inspection to confirm high-quality candidates. The detection algorithm flags a station(s), if the recorded *S* waveform(s) has(have) dominant period, wave energy, absolute peak amplitude to average amplitude ratio, and absolute peak delay (relative to *S* arrival) significantly larger than the median values of all stations analyzed. The computations are done on vertical and fault-parallel component velocity seismograms. After visual confirmation, waveforms from selected stations are inverted for parameters of the trapping structure using a genetic inversion algorithm with a forward kernel based on the analytical solution of Ben-Zion and Aki (1990) and Ben-Zion (1998). The topographic gradient to the northeast of the CF (Fig. 4) is not accounted for by the analytical solution; so, we expect an increased misfit during inversions related to stations atop this gradient compared to previous applications at other SJFZ arrays along flatter profiles (Qiu et al. 2017; Share et al. 2017; Qin et al. 2018).

4.3.2 Results

The automatic detection algorithm of Ross and Ben-Zion (2015) is applied on waveforms from local 143 earthquakes within a broad region that includes the SJFZ, San Andreas fault (SAF) and Elsinore fault (Fig. 10a). A search window for detecting FZTW is defined using the *S* picks described in Sect. 4.1. The automatic detector flags 194 potential FZTW from events throughout the region (Fig. 10a), with a maximum number of 4 picks made per event. The latter suggests that FZTW are most pronounced in waveforms recorded by $\geq$ 4 stations (as suggested in

Figs. 4, 5c). Approximately 80% of all detections are made for stations northeast of the CF trace (Fig. 10b).

We next visually inspect flagged FZTW. Seismograms are integrated to displacement prior to inspection and in preparation for waveform inversion. Subsequent to integration, the waveforms are convolved with $1/t^{1/2}$ to convert a point source response to that of an equivalent line dislocation source (e.g., Igel et al. 2002; Ben-Zion et al. 2003). Several events producing FZTW are confirmed through visual inspection and waveforms of two events (TW1 and TW2, Fig. 10a) are selected for inversion of fault zone properties. FZTW from these events appear most clearly (Figs. 11a, S3a) on fault-parallel rotated waveforms at stations around BS45 (106 m northeast of CF trace).

The forward model for the inversion consists of a fault zone layer sandwiched between two quarter spaces (Fig. 2 in Ben-Zion and Aki 1990). This basic model provides a useful modeling approach because it captures the key average geometrical and material properties affecting FZTW while accounting analytically for the strong trade-offs that exist between these parameters (Ben-Zion 1998). Various likely velocity gradients, internal scatterers and other small-scale heterogeneities in the trapping structure have small effects on FZTW that average out these heterogeneities (e.g., Igel et al. 1997; Jahnke et al. 2002). The inverted fault zone parameters are: (1–3) S velocities of the two quarter spaces (assumed different based on Sect. 4.2.2) and the fault zone layer, (4–5) width and Q value of the fault zone layer, (6) location of contact between the fault and left quarter space, and (7) propagation distance within the fault zone layer.

The genetic inversion algorithm maximizes the correlation between sets of synthetic seismograms calculated with the forward model and observed waveforms, while exploring systematically a large parameter space. This is accomplished by calculating fitness values associated with different sets of model parameters and migrating in the parameter space overall in the direction of larger fitness values. The fitness is defined as $(1 + C)/2$ where C is the correlation coefficient between synthetic and observed data. When C varies over the range -1 (perfect anti-correlation) to 1 (perfect correlation), the fitness value changes from 0 to 1. Only waveforms from stations BS34–58 (with noisy traces excluded) are inverted; this subset includes stations where FZTW are recorded and a sufficient number of stations to the northeast and southwest with no observed FZTW.

Synthetic waveforms (light blue lines in Fig. 11b) associated with the best-fit solution after 10,000 inversion iterations (black circles in Fig. 11c) are compared with recorded waveforms (black lines in Fig. 11b) from TW1. Summing the fitness values of the final 2000 inversion iterations (green dots in Fig. 11c) and normalizing the results to have unit sums give probability density functions for the various model parameters (curves in Fig. 11c). Corresponding inversion results for event TW2 are shown in Fig. S3. Because FZTW are generated by the same waveguide structure, inversions of waveforms associated with different high-quality candidates provide similar values for the most likely fault zone parameters. However, the parameters are subjected to significant trade-offs as discussed in previous studies (e.g., Ben-Zion 1998; Peng et al. 2003) and illustrated by the broad regions of high fitness values in Figs. 11c, S3c.

Based on the best-fit inversion results, the core damage zone is estimated to start at BS55 (main CF, Fig. 3b) and have width of $\sim$ 150 m, Q value of $\sim$ 40 and S velocity reduction of $\sim$ 55% relative to the bounding rocks. Event TW1 is beneath the array (Fig. 10a), so energy from the event propagates almost exclusively in the vertical direction and the best-fitting propagation distance of $\sim$ 2 km (Fig. 11c) reflects the depth extent of the core damage zone. On the other hand, event TW2 is located in the trifurcation area and FZTW generated by this event propagates a significant distance along-strike. Using for this event a propagation distance of 6 km (Fig. S3c) and a trapping structure depth of 2 km (Fig. 11c), the horizontal propagation distance within the waveguide from event TW2 is less than 6 km, considerably smaller than the epicentral distance of TW2 from the array (40 km, Fig. 10a). This indicates that the trapping structure does not extend continuously along-strike more than a few km, in agreement with inferences from other studies (e.g., Peng et al. 2003; Lewis and Ben-Zion 2010). For both

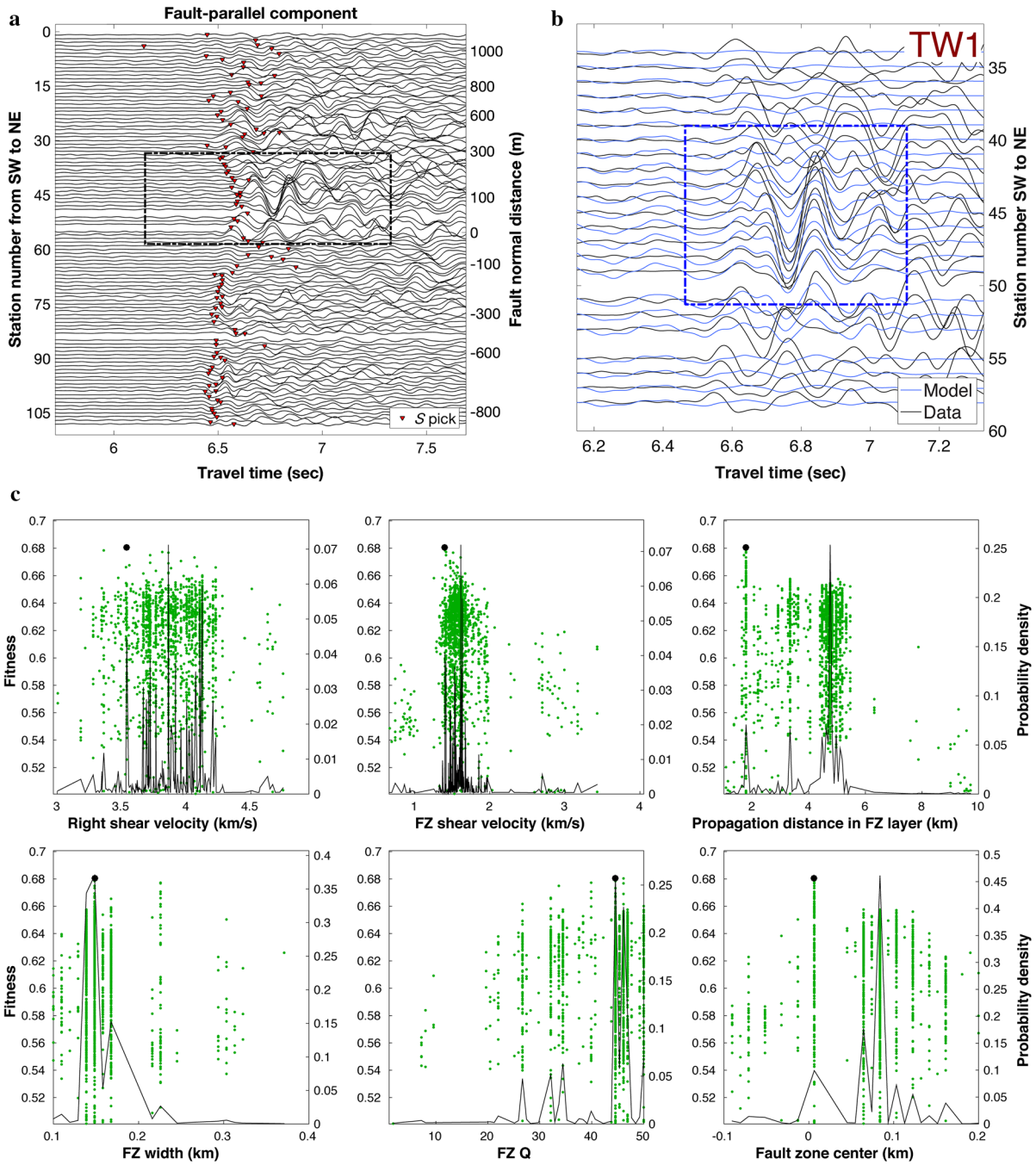

Figure 11

Fault model inversion results for event TW1. **a** Processed *S* waveforms (see text for processing steps) for the array with the dot-dashed box highlighting waveform analyzed during inversion. **b** Waveforms for stations BS34–58 (black traces) compared to synthetic waveforms (light blue traces) using fault parameters associated with the best-fit solution. The box shows the most pronounced FZTW. **c** Parameter space for the final 10 generations (2000 iterations). Green dots indicate fitness values for all solutions, black dots correspond to the best-fit solution and black lines are probability density curves of the inverted parameters

TW1 and TW2, the inversion yields an asymmetric damage zone centered northeast of the fault trace with near-zero probability of asymmetry in the other direction. Though the percent reduction in shear velocity is similar, the average velocity overall is higher for TW2, which is likely due to the difference in propagation distance along-fault.

5. Discussion

The performed analyses provide high-resolution imaging results on the damage zone and bimaterial interfaces in the structure of the Clark fault near Blackburn Saddle (BS) using a dense long-aperture linear array across the fault. The BS array has an order of magnitude larger aperture and number of stations than the earlier installed BB array (Share et al. 2017). Unlike other across-fault arrays (e.g., Schmandt and Clayton 2013; Ben-Zion et al. 2015), the BS array has three-component nodes recording at 1000-Hz sampling. This allows applications of high-resolution polarization analysis, accurate detection and modeling of *S*-type FZTW, and other tools that require dense arrays with three components of motion.

The denser spatiotemporal sampling over a significantly longer transect across the fault has several consequences for imaging the CF structure (Fig. 12). First, unlike the short BB array that covers only part of the damage zone, the longer BS array provides data that can be used to recover with teleseismic data (Fig. 4) the expected slowness profile across the entire damage zone (compare red and black profiles in Fig. 12a, top). Furthermore, comparisons between local *P* earthquake waveforms recorded within and outside the damage zone allow recognition of two different types of FZHW: head waves refracting along a deep bimaterial interface separating different crustal blocks across the CF (Fig. 12a, middle) and local FZHW propagating along the edge of the damage zone (Fig. 12a, bottom). The local FZHW were not analyzed in the earlier study using the BB array (Share et al. 2017) since that short array did not include stations outside the damage zone (Fig. 12b).

The results indicate that the main seismogenic CF at depth is close to its mapped surface trace (station

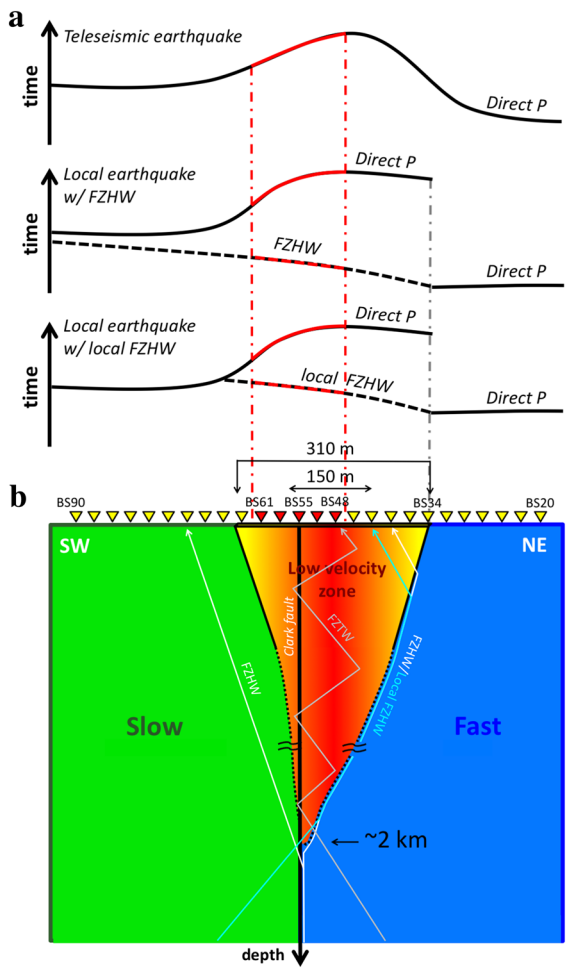

Figure 12
Schematic representation of arrival time variations of early *P* waves across the fault zone. **a** Expected variations in *P* first arrivals from teleseismic earthquakes (top), direct *P* and FZHW from on-fault local earthquakes (middle), and off-fault local earthquakes (bottom) given the fault model in **b**. The black lines represent profiles recorded by the BS array whereas the red profiles denote the limited profiles observed with the shorter BB array. The vertical gray dot-dashed line indicates abrupt changes in arrivals associated with a major bimaterial interface at the site and detected with the BS array only. **b** Simplified fault zone model suggested by analysis done in this work (not to scale) with nominally slow block on the southwest (green) separated from a fast block to the northeast (blue) by the main Clark fault (thick black line) and a low-velocity damage zone near the surface (warm colors with warmer representing greater damage). Fault zone parameters and example ray paths of several fault zone phases (white, gray and cyan lines) are indicated. Triangles on the surface show the BS array spanning the entire fault zone and red triangles mark the BB array covering only the southwestern side of the damage zone

BS55), and it manifests as abrupt changes in waveform character, inclination and linearity of teleseismic *P* waveforms (Figs. 3b, c, S1b). The large amplitude and delay time anomalies in teleseismic *P* arrivals (Fig. 4) and the presence of FZTW from local events (Figs. 5c, 11a, S3a) indicate an asymmetric damage zone (Fig. 12b) with a center 90–150 m (BS40–47) from the surface trace of the CF. The large-scale structural variation inferred from changes in waveforms recorded $\sim$ 270 m northeast of the CF (BS34, Figs. 3, 5b, S1) is most likely the northeastern edge of this damage zone (Fig. 12b). The analysis of teleseismic *P* arrivals reveals potential minor faults and associated damage outside (> 300 m from CF) the broader damage zone. These features are unresolved in our analyses and could be targets for a future study in the area.

A combination of high-resolution polarization, across- and along-fault move-out analyses applied to waveforms of local events reveals FZHW at locations southwest of BS34 and not northeast of that station (Fig. 7). These results suggest the broader damage zone is bounded to the northeast by a sharp bimaterial interface separating structure to the northeast that is on average faster than the structure to the southwest (Fig. 12b). The existence and sense of velocity contrast are supported by tomographic models (Allam and Ben-Zion 2012) and regional geology (e.g., Sharp 1967; Gutierrez et al. 2010; Salisbury et al. 2012). The results also suggest that the bimaterial interface merges with the CF at depth and is continuous for at least 50 km to the southeast, as the observed FZHW are generated by events located within and beyond the trifurcation area (Fig. 8a). This implies the CF is continuous at depth through the Anza seismic gap and over a larger distance than previously estimated (Share et al. 2017), highlighting the potential for large earthquake rupture through the region as suggested by paleoseismic studies (Rockwell et al. 2015).

A *P*-wave velocity contrast in the range $\sim$ 11–23% across the damage zone is calculated from the differential time between local FZHW propagating at the edge of the damage zone and direct *P* waves (Fig. 9c). This range of *P* velocity contrast corresponds to the *S* velocity contrast across the trapping structure derived from analysis of FZTW, assuming V_P/V_S ratios in the range 2.95–3.45 that may represent shallow damage rocks (e.g., O'Connell and Budiansky 1974; Mavko et al. 1998). Similar near-surface contrasts across the SJFZ are observed at a site $\sim$ 50 km to the southeast (Qiu et al. 2017). An average velocity contrast of 11.2% across a deep section of the CF around the trifurcation area is calculated from the move-out between FZHW and direct *P* waves with along-fault distance (Fig. 8c). These values are comparable to contrasts across the SAF south of Hollister (McGuire and Ben-Zion 2005) and sections of the Hayward fault (Allam et al. 2014). A similar contrast of 9.2% is derived from velocities 1.5 km on either side of the trifurcation area CF up to 10-km depth (median depth of events generating FZHW) in the V_P model of Allam and Ben-Zion (2012). The smaller velocity contrast observed for the CF at depth closer to the array is, in turn, comparable to results for the SAF around San Gorgonio Pass (Share and Ben-Zion 2016) and North Anatolian fault (Najdahmadi et al. 2016). The observed FZHW indicate the existence of a continuous sharp bimaterial interface in the core structure of the CF, between the generating events and the BS array (Fig. 8a), despite structural discontinuities at the surface (Sanders and Magistrale 1997) and irrespective of (lateral and/or vertical) changes in the velocity structure.

Properties of the fault damage zone are obtained from delay time analysis and inversions of FZTW following *S* arrivals. The extent of the broader damage zone is inferred from the number of stations that record teleseismic *P* arrivals with above-average delay and local FZHW (Sects. 3.2, 4.2.2). Relative to the median delay (horizontal dot-dashed line Fig. 4b), stations BS35–61 consistently have larger delay times for all events and reference velocities considered. These stations, therefore, overlie a region of above-average slowness. The same set of stations also record local FZHW (Fig. 7, 4th row). This implies the damage zone edge(s) along which local FZHW propagate locate northeast of BS35 and southwest of BS61. We, therefore, estimate the width of the broader damage zone to be comparable to the 310-m-wide zone spanning these stations (Fig. 12b). Along the Parkfield section of the SAF, observations of FZHW similarly reveal the extent of a broad damage zone that is asymmetric with respect to the main fault

trace (Li and Peng 2016). Inversions of waveforms with FZTW provide information on the fault zone trapping structure within this broader damage zone. The results indicate (Figs. 11c, S3c) a trapping structure that extends < 6 km along-strike and to a depth of 2 km based on the best-fit propagation distances from the FZTW inversions. The trapping structure is about 150 m wide and has S velocity reduction of 55% and Q value of about 40. These parameters are similar to properties of trapping structures along other sections of the SJFZ (Lewis et al. 2005; Qiu et al. 2017; Qin et al. 2018), SAF at Parkfield (Lewis and Ben-Zion 2010), Karadere branch of the North Anatolian fault (Ben-Zion et al. 2003) and other active strike-slip faults and rupture zones. The larger-aperture BS array (compared to BB, Figs. 3a, 5a) allows for better resolution of the trapping structure within the broader damage zone, and the properties estimated here (Figs. 11c, S3c) are, therefore, more accurate than those reported in Share et al. (2017).

The sense of velocity contrast across the CF at depth towards the southeast (Fig. 8), combined with results on bimaterial ruptures (e.g., Weertman 1980; Andrews and Ben-Zion 1997; Brietzke et al. 2009; Shlomai and Fineberg 2016), suggest that earthquakes in that fault section tend to propagate to the northwest. This is consistent with studies on directivity of small–moderate events along the CF between the trifurcation area and the BS array (Kurzon et al. 2014; Ross and Ben-Zion 2016). Persistent occurrence of bimaterial ruptures with preferred propagation direction is expected to produce more damage on the side with faster velocity at depth (Ben-Zion and Shi 2005). This agrees with the geological mapping of Dor et al. (2006) near Anza, and the observed damage asymmetry across the CF to the northeast (Figs. 4, 5, 9, 11) summarized in Fig. 12b. Similar asymmetric damage zones are also associated with CF at sites southeast of Blackburn Saddle (Qiu et al. 2017; Qin et al. 2018). A recent example of both rupture directivity and damage asymmetry across the CF is provided by the June 2016 M_W 5.2 Borrego Springs earthquake, where rupture initiated in the trifurcation area, propagated to the northwest and generated significantly more aftershocks (damage) northeast of the fault (Ross et al. 2017a, b).

The results of this work are obtained by a set of separate analyses that examine different phases with different techniques and largely ignore the topography (other than travel time corrections). A more complete analysis that merges the detailed fault zone structure within a larger-scale tomographic model and accounts for topography may be done with 3D numerical simulations of the type explored by Allam et al. (2015). This approach is computationally very demanding but is currently feasible. Additional information about the fault zone structure may be obtained by analyzing the ambient seismic noise recorded by the dense linear array (e.g., Hillers et al. 2014). These studies may be the subject of future work.

Acknowledgements

We thank Marianne Karplus and Jerry Schuster for providing geophones for the experiment, and Hsin-Hua Huang, Elizabeth Berg, Yadong Wang, Scott Palmer, Kathleen Ritterbush, Jon Gonzalez, Jerry Schuster, Robert Zinke and Cooper W. Harris for assistance during the array deployment. The research was supported by the King Abdullah University of Science and Technology (Award OCRF-2014-CRG3-2300), the National Science Foundation (Grants CyberSEES-1442665 and EAR-1620601), and the Department of Energy (Awards DESC0016520 and DE-SC0016527). The data collected with the BS array are stored at the University of Utah Seismograph Stations and are available upon request. Most maps are made using the Generic Mapping Tools (Wessel et al. 2013). The manuscript benefitted from useful comments by two anonymous referees.

References

Allam, A., & Ben-Zion, Y. (2012). Seismic velocity structures in the southern California plate boundary environment from double difference tomography. *Geophysical Journal International, 190,* 1181–1196.

Allam, A. A., Ben-Zion, Y., & Peng, Z. (2014). Seismic imaging of a bimaterial interface along the Hayward fault, CA, with fault

zone head waves and Direct P arrivals. *Pure and Applied Geophysics, 171*(11), 2993–3011.

Allam, A. A., Tape, C., & Ben-Zion, Y. (2015). Finite-frequency sensitivity kernels of seismic waves to fault zone structures. *Geophysical Journal International, 203,* 2032–2048. https://doi.org/10.1093/gji/ggv413.

Andrews, D. J., & Ben-Zion, Y. (1997). Wrinkle-like slip pulse on a fault between different materials. *Journal of Geophysical Research, 102,* 553–571.

Barak, S., Klemperer, S. L., & Lawrence, J. F. (2015). San Andreas fault dip, peninsular ranges mafic lower crust and partial melt in the Salton Trough, Southern California, from ambient–noise tomography. *Geochemistry, Geophysics, Geosystems*. https://doi.org/10.1002/2015GC005970.

Ben-Zion, Y. (1989). The response of two joined quarter spaces to SH line sources located at the material discontinuity interface. *Geophysical Journal International, 98,* 213–222.

Ben-Zion, Y. (1998). Properties of seismic fault zone waves and their utility for imaging low-velocity structures. *Journal of Geophysical Research, 103,* 12567–12585.

Ben-Zion, Y., & Aki, K. (1990). Seismic radiation from an SH line source in a laterally heterogeneous planar fault zone. *Bulletin of the Seismological Society of America, 80,* 971–994.

Ben-Zion, Y., Katz, S., & Leary, P. (1992). Joint inversion of fault zone head waves and direct P arrivals for crustal structure near major faults. *Journal of Geophysical Research, 97,* 1943–1951.

Ben-Zion, Y., Peng, Z., Okaya, D., Seeber, L., Armbruster, J. G., Ozer, N., et al. (2003). A shallow fault-zone structure illuminated by trapped waves in the Karadere–Duzce branch of the North Anatolian Fault, western Turkey. *Geophysical Journal International, 152*(3), 699–717.

Ben-Zion, Y., & Shi, Z. (2005). Dynamic rupture on a material interface with spontaneous generation of plastic strain in the bulk. *Earth and Planetary Science Letters, 236*(1), 486–496.

Ben-Zion, Y., Vernon, F., Ozakin, Y., Zigone, D., Ross, Z., Meng, H., et al. (2015). Basic data features and results from a spatially dense seismic array on the San Jacinto fault zone. *Geophysical Journal International, 202,* 370–380.

Brietzke, G. B., Cochard, A., & Igel, H. (2009). Importance of bimaterial interfaces for earthquake dynamics and strong ground motion. *Geophysical Journal International, 178,* 921–938.

Bulut, F., Ben-Zion, Y., & Bonhoff, M. (2012). Evidence for a bimaterial interface along the Mudurnu segment of the North Anatolian Fault Zone from polarization analysis of P waves. *Earth and Planetary Science Letters, 327–328,* 17–22.

Cochran, E. S., Li, Y.-G., Shearer, P. M., Barbot, S., Fialko, Y., & Vidale, J. E. (2009). Seismic and geodetic evidence for extensive, long-lived fault damage zones. *Geology, 37*(4), 315–318.

Crotwell, H. P., Owens, T. J., & Ritsema, J. (1999). The TauP Toolkit: Flexible seismic travel-time and ray-path utilities. *Seismological Research Letters, 70*(2), 154–160.

DeDontney, N., Templeton-Barrett, E. L., Rice, J. R., & Dmowska, R. (2011). Influence of plastic deformation on bimaterial fault rupture directivity. *Journal of Geophysical Research, 116,* B10312. https://doi.org/10.1029/2011JB008417.

Dor, O., Rockwell, T. K., & Ben-Zion, Y. (2006). Geological observations of damage asymmetry in the structure of the San Jacinto, San Andreas and Punchbowl Faults in Southern California: A possible indicator for preferred rupture propagation direction. *Pure and Applied Geophysics, 163,* 301–349.

Dor, O., Yildirim, C., Rockwell, T. K., Ben-Zion, Y., Emre, O., Sisk, M., et al. (2008). Geological and geomorphologic asymmetry across the rupture zones of the 1943 and 1944 earthquakes on the North Anatolian Fault: Possible signals for preferred earthquake propagation Direction. *Geophysical Journal International, 173,* 483–504.

Eccles, J. D., Gulley, A. K., Malin, P. E., Boese, C. M., Townend, J., & Sutherland, R. (2015). Fault Zone Guided Wave generation on the locked, late interseismic Alpine Fault, New Zealand. *Geophysical Research Letters, 42*(14), 5736–5743.

Fang, H., Zhang, H., Yao, H., Allam, A., Zigone, D., Ben-Zion, Y., et al. (2016). A new three-dimensional joint inversion algorithm of body-wave and surface-wave data and its application to the Southern California Plate Boundary Region. *Journal of Geophysical Research, 121*(5), 3557–3569.

Gutierrez, C., Bryant, W., Saucedo, W.G., & Wills, C. (2010). Geologic map of California, California Geological Survey.

Hadley, D., & Kanamori, H. (1977). Seismic structure of the Transverse Ranges, California. *Geological Society of America Bulletin, 88,* 1469–1478.

Hauksson, E., Yang, W., & Shearer, P. M. (2012). Waveform relocated earthquake catalog for southern California (1981 to June 2011). *Bulletin of the Seismological Society of America, 102*(5), 2239–2244.

Hillers, G., Campillo, M., Ben-Zion, Y., & Roux, P. (2014). Seismic fault zone trapped noise. *Journal of Geophysical Research, 119*(7), 5786–5799.

Hillers, G., Roux, P., Campillo, M., & Ben-Zion, Y. (2016). Focal spot imaging based on zero lag cross correlation amplitude fields: Application to dense array data at the San Jacinto fault zone. *Journal of Geophysical Research*. https://doi.org/10.1002/2016JB013014.

Igel, H., Ben-Zion, Y., & Leary, P. C. (1997). Simulation of *SH*- and *P-SV*-wave propagation in fault zones. *Geophysical Journal International, 128*(3), 533–546.

Igel, H., Jahnke, G., & Ben-Zion, Y. (2002). Numerical simulation of fault zone guided waves: Accuracy and 3-D effects. *Pure and Applied Geophysics, 159,* 2083–2967.

Jahnke, G., Igel, H., & Ben-Zion, Y. (2002). Three-dimensional calculations of fault-zone-guided waves in various irregular structures. *Geophysical Journal International, 151*(2), 416–426.

Jepsen, D. C., & Kennett, B. L. N. (1990). Three component analysis of regional seismograms. *Bulletin of the Seismological Society of America, 80,* 2032–2052.

Jurkevics, A. (1988). Polarization analysis of three-component array data. *Bulletin of the Seismological Society of America, 78*(5), 1725–1743.

Kennett, L. N. (1991). IASPEI 1991 Seismological Tables. *Bibliotech, 167.*

Kurzon, I., Vernon, F. L., Ben-Zion, Y., & Atkinson, G. (2014). Ground motion prediction equations in the San Jacinto Fault Zone—Significant effects of rupture directivity and fault zone amplification. *Pure and Applied Geophysics, 171,* 3045–3081.

Lewis, M. A., & Ben-Zion, Y. (2010). Diversity of fault zone damage and trapping structures in the Parkfield section of the San Andreas Fault from comprehensive analysis of near fault seismograms. *Geophysical Journal International, 183*(3), 1579–1595.

Lewis, M. A., Ben-Zion, Y., & McGuire, J. (2007). Imaging the deep structure of the San Andreas Fault south of Hollister with

joint analysis of fault-zone head and Direct P arrivals. *Geophysical Journal International, 169,* 1028–1042.

Lewis, M. A., Peng, Z., Ben-Zion, Y., & Vernon, F. L. (2005). Shallow seismic trapping structure in the San Jacinto fault zone near Anza, California. *Geophysical Journal International, 162,* 867–881.

Li, Y.-G., Aki, K., Adams, D., Hasemi, A., & Lee, W. H. K. (1994). Seismic guided waves trapped in the fault zone of the Landers, California, earthquake of 1992. *Journal of Geophysical Research, 99,* 11705–11722.

Li, Y.-G., & Leary, P. C. (1990). Fault zone trapped seismic waves. *Bulletin of the Seismological Society of America, 80*(5), 1245–1271.

Li, Z., & Peng, Z. (2016). Automatic identification of fault zone head waves and direct *P* waves and its application in the Parkfield section of the San Andreas Fault. *Geophysical Journal International, 205,* 1326–1341.

Mavko, G., Mukerji, T., & Dvorkin, J. (1998). *The rock physics handbook: Tools for seismic analysis in porous media* (p. 329). Cambridge, UK: Cambridge University Press.

McGuire, J., & Ben-Zion, Y. (2005). High-resolution imaging of the Bear Valley section of the San Andreas Fault at seismogenic depths with fault-zone head waves and relocated seismicity. *Geophysical Journal International, 163,* 152–164.

Mizuno, T., & Nishigami, K. (2006). Deep structure of the Nojima fault, southwest Japan, estimated from borehole observation of fault-zone trapped waves. *Tectonophysics, 417,* 231–247.

Najdahmadi, B., Bohnhoff, M., & Ben-Zion, Y. (2016). Bimaterial interfaces at the Karadere segment of the North Anatolian Fault, northwestern Turkey. *Journal of Geophysical Research, 121,* 931–950.

Neuberg, J., & Pointer, T. (2000). Effects of volcano topography on seismic broad-band waveforms. *Geophysical Journal International, 143,* 239–248.

O'Connell, R. J., & Budiansky, B. (1974). Seismic velocities in dry and saturated cracked solids. *Journal of Geophysical Research, 79*(35), 5412–5426.

Oppenheimer, D. H., Reasenberg, P. A., & Simpson, R. W. (1988). Fault plane solutions for the 1984 Morgan Hill, California, earthquake sequence: evidence for the state of stress on the Calaveras fault. *Journal of Geophysical Research, 143,* 239–248.

Peng, Z., Ben-Zion, Y., Michael, A. J., & Zhu, L. (2003). Quantitative analysis of seismic trapped waves in the rupture zone of the 1992 Landers, California earthquake: Evidence for a shallow trapping structure. *Geophysical Journal International, 155,* 1021–1041.

Qin, L., Ben-Zion, Y., Qiu, H., Share, P.-E., Ross, Z. E., & Vernon, F. (2018). Internal structure of the San Jacinto fault zone in the trifurcation area southeast of Anza, California, from data of dense seismic arrays. *Geophysical Journal International, 213,* 98–114. https://doi.org/10.1093/gji/ggx540.

Qiu, H., Ben-Zion, Y., Ross, Z. E., Share, P.-E., & Vernon, F. (2017). Internal structure of the San Jacinto fault zone at Jackass Flat from data recorded by a dense linear array. *Geophysical Journal International, 209*(3), 1369–1388.

Ringler, A. T., Anthony, R. E., Karplus, M. S., Holland, A. A., & Wilson, D. C. (2018). Laboratory tests of three Z-land Fairfield Nodal 5-Hz, three component sensors. *Seismological Research Letters*. https://doi.org/10.1785/0220170236.

Rockwell, T. K., Dawson, T. E., Young-Ben Horton, J., & Seitz, G. (2015). A 21 event, 4000-year history of surface ruptures in the Anza Seismic Gap, San Jacinto Fault and implications for long-term earthquake production on a major plate boundary fault. *Pure and Applied Geophysics, 172*(5), 1143–1165.

Ross, Z. E., & Ben-Zion, Y. (2014). Automatic picking of Direct P, S seismic phases and fault zone head waves. *Geophysical Journal International, 199,* 368–381.

Ross, Z. E., & Ben-Zion, Y. (2015). An algorithm for automated identification of fault zone trapped waves. *Geophysical Journal International, 202,* 933–942.

Ross, Z. E., & Ben-Zion, Y. (2016). Toward reliable automated estimates of earthquake source properties from body wave spectra. *Journal of Geophysical Research*. https://doi.org/10.1002/2016JB013003.

Ross, Z. E., Hauksson, E., & Ben-Zion, Y. (2017a). Abundant off-fault seismicity and orthogonal structures in the San Jacinto fault zone. *Science Advances, 3,* e1601946.

Ross, Z. E., Kanamori, H., & Hauksson, E. (2017b). Anomalously large complete stress drop during the 2016 M_W 5.2 Borrego Springs earthquake inferred by waveform modeling and near-source aftershock deficit. *Geophysical Research Letters, 44,* 5994–6001.

Ross, Z. E., White, M. C., Vernon, F. L., & Ben-Zion, Y. (2016). An improved algorithm for real-time S-wave picking with application to the (augmented) ANZA network in Southern California. *Bulletin of the Seismological Society of America, 106*(5), 2013–2022.

Salisbury, J. B., Rockwell, T. K., Middleton, T. J., & Hudnut, K. W. (2012). LiDAR and field observations of slip distribution for the most recent surface ruptures along the central San Jacinto Fault. *Bulletin of the Seismological Society of America, 102*(2), 598–619.

Sanders, C. O., & Kanamori, H. (1984). A seismotectonic analysis of the Anza seismic gap, San Jacinto fault zone, southern California. *Journal of Geophysical Research, 89*(B7), 5873–5890.

Sanders, C., & Magistrale, H. (1997). Segmentation of the northern San Jacinto fault zone, southern California. *Journal of Geophysical Research, 102*(B12), 27453–27467.

SCEDC. (2013). *Southern California Earthquake Data Center*. Caltech: Dataset. https://doi.org/10.7909/C3WD3xH.

Schmandt, B., & Clayton, R. W. (2013). Analysis of teleseismic P waves with a 5200-station array in Long Beach, California: Evidence for an abrupt boundary to Inner Borderland rifting. *Journal of Geophysical Research, 118,* 1–19.

Share, P.-E., & Ben-Zion, Y. (2016). Bimaterial interfaces in the South San Andreas Fault with opposite velocity contrasts NW and SE from San Gorgonio Pass. *Geophysical Research Letters*. https://doi.org/10.1002/2016GL070774.

Share, P.-E., Ben-Zion, Y., Ross, Z. E., Qiu, H., & Vernon, F. (2017). Internal structure of the San Jacinto fault zone at Blackburn Saddle from seismic data of a linear array. *Geophysical Journal International, 210*(2), 819–832.

Sharp, R. V. (1967). San Jacinto fault zone in the peninsular ranges of Southern California. *Geological Society of America Bulletin, 78*(6), 705–730.

Shlomai, H., & Fineberg, J. (2016). The structure of slip-pulses and supershear ruptures driving slip in bimaterial friction. *Nature Communications, 7,* 11787.

Sibson, R. H. (1989). Earthquake faulting as a structural process. *Journal of Structural Geology, 11,* 1–14.

Weertman, J. (1980). Unstable slippage across a fault that separates elastic media of different elastic constants. *Journal of Geophysical Research, 85,* 1455–1461.

Wessel, P., Smith, W. H. F., Scharroo, R., Luis, J. F., & Wobbe, F. (2013). Generic mapping tools: improved version released. *EOS Transactions of the American Geophysical Union, 94,* 409–410.

Xu, S., Ben-Zion, Y., & Ampuero, J. P. (2012). Properties of inelastic yielding zones generated by in-plane dynamic ruptures-II. Detailed parameter-space study. *Geophysical Journal International, 191*(3), 1343–1360.

Yang, H., Li, Z., Peng, Z., Ben-Zion, Y., & Vernon, F. (2014). Low velocity zones along the San Jacinto Fault, Southern California, from body waves recorded in dense linear arrays. *Journal of Geophysical Research, 119,* 8976–8990.

Yang, W., Peng, Z., Wang, B., Li, Z., & Yuan, S. (2015). Velocity contrast along the rupture zone of the 2010 Mw6.9 Yushu, China, earthquake from fault zone head waves. *Earth and Planetary Science Letters, 416,* 91–97.

(Received May 27, 2018, revised August 27, 2018, accepted September 3, 2018, Published online September 18, 2018)